Application of BEM (boundary element method)-based acoustic holography to radiation analysis of sound sources with arbitrarily shaped geometries

Mingsian R. Bai

Department of Mechanical Engineering, National Chiao Tung University, 1001 Ta Hsueh Road, Hsin Chu 30050, Taiwan, Republic of China

A method employing holograms that conform with arbitrarily shaped sources has been developed for enhancing conventional near-field acoustic holography, which has been limited to sources with simple geometries, e.g., planar or cylindrical surfaces. Four holography transformation algorithms have been developed, based on acoustic holography theory and the boundary element method (BEM). Singular value decomposition (SVD) has been incorporated into the algorithms in order to alleviate the ill-posed nature frequently encountered in backward reconstruction of a field. A pulsating sphere, a cylinder with spherical endcaps, and a vibrating piston set in a rigid sphere have been adopted in a numerical simulation for verifying the algorithms. Satisfactory agreement has been achieved between the holographically transformed results and the analytical solutions.

INTRODUCTION

Acoustic holography, as its name suggests, provides the capability of projecting an image in a three-dimensional space, based on the sound data measured on a two-dimensional hologram surface, by virtue of spatial transformation algorithms. A two-dimensional fast Fourier transform (FFT) algorithm has been utilized in the past for efficiently carrying out computations involved in holography transformation. Maynard *et al.* used the FFT approach in reconstruction of sound fields for planar sources.[1,2] The same approach was then extended to deal with cylindrical sources by Williams and Dardy.[3] The FFT-based algorithm, in spite of its efficiency, has been limited to source surfaces (as well as holograms) with simple geometries, for example, planar and cylindrical surfaces. This requirement, however, has not always been met in many industrial applications where irregularly shaped sound sources have been present. Under these circumstances, methods of eigenexpansion have generally not been possible for performing spatial transformation. It has become desirable to extend planar holography for reconstruction of sound fields generated by irregularly shaped sources. Veronesi and Maynard[4] first noted this need for generalization of near-field acoustic holography, suggesting a holography transformation method for reconstruction of sound fields radiated by irregularly shaped sources. Their method was based on a somewhat primitive discretization scheme involving the use of constant elements for approximating field variables. The boundary element method (BEM), developed by Huang,[5] was an improvement on their method. The present research, along the same lines as the previous work, was conducted through an extensive numerical simulation to investigate the transformation parameters; it also illustrates an entire implementation process which might benefit future researchers.

A BEM-based acoustic holography technique is devel-oped in this study for reconstruction of sound fields genera-ted by irregularly shaped sources. Four numerical schemes are implemented to perform the required spatial transforma-tion. Ill-posed nature resulting from backward reconstruc-tion of source fields is also dealt with through the use of the singular value decomposition (SVD) algorithm. A pulsat-ing sphere, a cylinder with spherical endcaps, and a vibrating piston set in a rigid sphere are chosen as the test sound sources in a numerical simulation. This is done in order to verify the BEM-based acoustic holography algorithms. Ob-servations obtained from a comparison between the analyti-cal solutions and the holographically transformed results will be commented on in the conclusion.

I. INTEGRAL FORMULATION OF SOUND RADIATION PROBLEMS

A brief review of the integral formulation of acoustic radiation problems is given in this section to facilitate the development of the BEM-based acoustic holography algo-rithms.

From linear acoustics, a monochromatic sound field is governed by the Helmholtz equation:[6]

$$(\nabla^2 + k^2)p(\mathbf{x}) = 0, \tag{1}$$

with boundary conditions specified on the source surface, where k is the wave number and p is the sound pressure. From the theory of Green's functions, Eq. (1) can be recast into the Helmholtz integral for an exterior boundary value problem:[7,8]

$$\alpha p(\mathbf{x}_p) = \int_{S_s} \left(p(\mathbf{x}_q) \frac{\partial}{\partial n_q} G(\mathbf{x}_p, \mathbf{x}_q) \right.$$
$$\left. - G(\mathbf{x}_p, \mathbf{x}_q) \frac{\partial p}{\partial n_q}(\mathbf{x}_q) \right) dS_q, \tag{2}$$

where S_s denotes the source surface; $\mathbf{x}_p$ and $\mathbf{x}_q$ are, respectively, the field point and the source point; $G(\mathbf{x}_p,\mathbf{x}_q) = e^{ikr}/4\pi r$ is the free-space Green's function corresponding to the Helmholtz equation; $\partial/\partial n_q \equiv \mathbf{n}_q \cdot \nabla$ ($\mathbf{n}_q$ denotes the outward normal to the source surface S_s);

$$\alpha = \begin{cases} 1, & \mathbf{x}_p \in V, \\ 0, & \mathbf{x}_p \in V_s, \\ \tfrac{1}{2}, & \mathbf{x}_p \in S_s, S_s \text{ a smooth surface,} \\ \Omega/4\pi, & \mathbf{x}_p \in S_s, S_s \text{ a nonsmooth surface} \\ & (\Omega \text{ is the solid angle}).^8 \end{cases}$$

Equation (2) requires the sound pressure p and its gradient $\partial p/\partial n$ on the surface to be related as if they correspond to a field generated solely by sources within an enclosed volume. The following Sommerfeld radiation condition has also been incorporated in the derivation of Eq. (2):[7,8]

$$\lim_{r \to \infty} r\left(\frac{\partial p}{\partial n} - ikp\right) = 0. \tag{3}$$

Equation (2) can be written in a more succinct form by means of operator notations:[9–11]

$$\alpha p(\mathbf{x}_p) = (Dp)(\mathbf{x}_p) - \left(S\frac{\partial p}{\partial n_q}\right)(\mathbf{x}_p), \tag{4}$$

where

$$\left(S\frac{\partial p}{\partial n_q}\right)(\mathbf{x}_p) \equiv \int_{S_s} G(\mathbf{x}_p,\mathbf{x}_q)\,\frac{\partial p}{\partial n_q}(\mathbf{x}_q)dS_q,$$

is the representation of a single layer potential and

$$(Dp)(\mathbf{x}_p) \equiv \int_{S_s} \frac{\partial}{\partial n_q} G(\mathbf{x}_p,\mathbf{x}_q)p(\mathbf{x}_q)dS_q,$$

is the representation of a double layer potential. Equation (4) can also be differentiated with respect to an arbitrary direction $\mathbf{n}_p$ to yield

$$\alpha\frac{\partial p}{\partial n_p}(\mathbf{x}_p) = \int_{S_s}\left(p(\mathbf{x}_q)\frac{\partial^2}{\partial n_p \partial n_q} G(\mathbf{x}_p,\mathbf{x}_q)\right.$$
$$\left. - \frac{\partial}{\partial n_p} G(\mathbf{x}_p,\mathbf{x}_q)\frac{\partial}{\partial n_q}p(\mathbf{x}_q)\right)dS_q, \tag{5}$$

or

$$\frac{\partial p}{\partial n_p}(\mathbf{x}_p) = (D_n p)(\mathbf{x}_p) - \left(K\frac{\partial p}{\partial n_q}\right)(\mathbf{x}_p), \tag{6}$$

where

$$\left(K\frac{\partial p}{\partial n_q}\right)(\mathbf{x}_p) \equiv \int_{S_s}\frac{\partial}{\partial n_p} G(\mathbf{x}_p,\mathbf{x}_q)\frac{\partial}{\partial n_q}p(\mathbf{x}_q)dS_q,$$

$$(D_n p)(\mathbf{x}_p) \equiv \int_{S_s}\frac{\partial^2}{\partial n_p \partial n_q} G(\mathbf{x}_p,\mathbf{x}_q)p(\mathbf{x}_q)dS_q,$$

where $[K(\partial p/\partial n_q)](\mathbf{x}_p)$ and $(D_n p)(\mathbf{x}_p)$ are, respectively, the partial derivatives of $[S(\partial p/\partial n_q)](\mathbf{x}_p)$ and $(Dp)(\mathbf{x}_p)$ with respect to $\mathbf{n}_p$. Here, the Euler's equation can be used to determine the particle velocity based on the known pressure gradient $\partial p(\mathbf{x}_p)/\partial n_p$:

$$v_n(\mathbf{x}_p) = \frac{1}{i\rho\omega}\frac{\partial}{\partial n_p}p(\mathbf{x}_p). \tag{7}$$

The sound pressure $p(\mathbf{x}_p)$ and the particle velocity $v_n(\mathbf{x}_p)$ then lead directly to the active intensity I_n and reactive intensity Q_n:

$$I_n(\mathbf{x}_p) = \tfrac{1}{2}\mathrm{Re}[p(\mathbf{x}_p)v_n(\mathbf{x}_p)^*] \tag{8}$$

and

$$Q_n(\mathbf{x}_p) = \tfrac{1}{2}\mathrm{Im}[p(\mathbf{x}_p)v_n(\mathbf{x}_p)^*], \tag{9}$$

where Re and Im denote the real part and the imaginary part, with * denoting complex conjugate.

Boundary integral equations (4) and (6) form the basis of sound radiation analysis for irregularly shaped sources. Suppose that either the sound pressure p or the pressure gradient $\partial p/\partial n$ on the source surface S_s is known *a priori*. Equation (4) or (6) can then be used to calculate the other quantity by assigning α the value of 1/2 or $\Omega/4\pi$, depending on whether the source boundary of concern is smooth or not. If the acoustic variables at some field point in the space are further desired, Eqs. (4) and (6) can again be used to propagate the previously determined boundary data to any field point of interest by assigning α the value of unity. These integral formulations will be used in the following section for deriving various BEM-based acoustic holography algorithms.

II. DEVELOPMENT OF BEM-BASED ACOUSTIC HOLOGRAPHY ALGORITHMS

Consider a sound source of finite volume V_s, bounded by a piecewise continuous surface S_s (see Fig. 1). A source radiates acoustic energy to an infinite domain V, with the Sommerfeld radiation condition imposed at infinity. Assume that one is only able to measure sound data on the hologram S_h which separates the volume V into two parts: V_b and V_f. Holography transformation consists of two types of processes: backward reconstruction and forward propa-

$$(\nabla^2 + k^2)\ p = 0$$
$$\text{in } V = V_f + V_b$$

$\mathbf{x}_q$: Source point
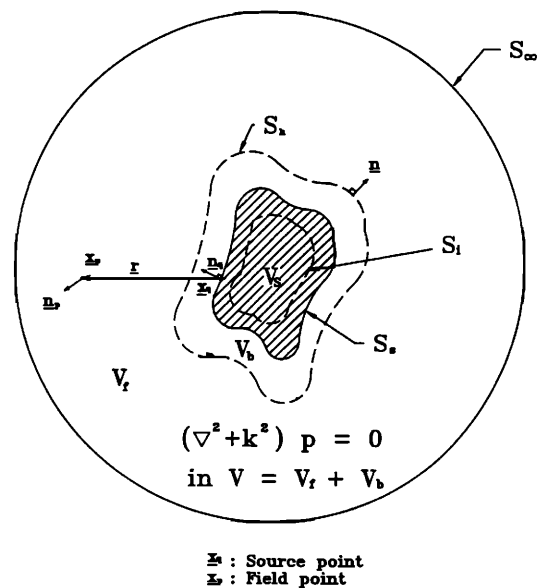$\mathbf{x}_p$: Field point

FIG. 1. Schematics for an exterior boundary value problem of acoustic holography transformation.

gation. In backward reconstruction, one essentially propagates the hologram data measured on S_h inward to a point of interest in the near field V_b or on the source surface S_s. In forward propagation, one propagates the hologram data measured on S_h outward to a point of interest in the far field V_f. A fundamental difference between a typical boundary element problem and a holography transformation problem is readily observed from the problem statement. The field on the source surface can be solved by typical boundary element methods[12,13] for boundary value problems of sound radiation when sound data are prescribed on the source surface S_s. On the other hand, for the acoustic holography problem discussed in this paper, one seeks to determine the sound field in a three-dimensional space, based on either the sound pressure or the pressure gradient measured on a hologram (since the sound data on the source surface are assumed to be difficult to access). It is then highly desirable to develop spatial transformation algorithms that are capable of the backward reconstruction of the sound pressure and pressure gradient on the source surface, and also of the forward propagation of the reconstructed source field to the field points of interest in a three-dimensional space. The boundary element method is adopted in this study as a building block for implementation of four kinds of holography transformation algorithms for sound fields radiated by irregularly shaped sources. A brief review of the boundary element method, in conjunction with the development of the holography transformation technique, is given in the following discussion.

A. Discretization of boundary integral equations

The numerical method employed for solving the acoustic holography problem in this study is the boundary element method which has been widely used in the area of acoustic radiation and scattering.[14-18] There are numerous advantages to using the boundary element method for solving exterior acoustic radiation problems. The boundary element method, in comparison with the finite difference method and the finite element method, requires less memory space since the dimensionality of a problem is reduced by one. The boundary condition at infinity, i.e., the Sommerfeld radiation condition, is already incorporated into the boundary integral formulation, while the condition at infinity always poses difficulties for the other two numerical methods. The boundary element method, in contrast to the FFT method used in conventional planar or cylindrical holography, provides more flexibility in choosing the spacing between measurement points and the shape of the conformal hologram.

The boundary elements used for approximating the surface integral are schematically shown in Fig. 2. Triangular elements and quadrilateral elements are used in this study for construction of meshes. The global coordinate system and local coordinate system are related by isoparametric transformation. Quadratic shape functions are used for interpolating the global coordinates, the sound pressure, and the pressure gradient on the source boundary as

$$X_i(\xi) = \sum_{l=1}^{L} N_l(\xi) x_{il}, \quad i = 1,2,3; \quad L = 6 \text{ or } 8, \quad (10)$$
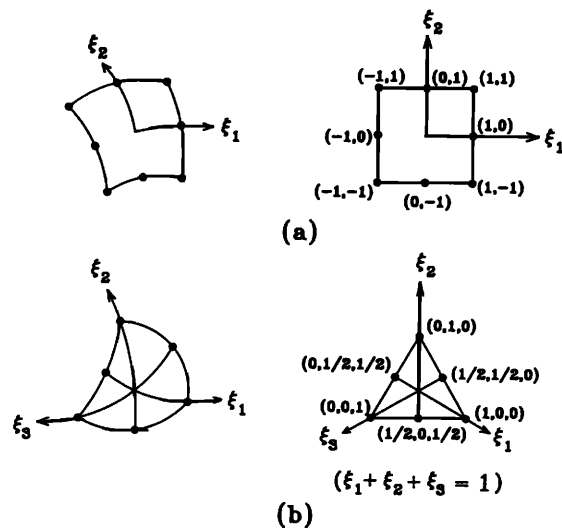

FIG. 2. Boundary elements used in isoparametric transformation. (a) Quadratic quadrilateral element; (b) quadratic triangular element.

$$P_m(\xi) = \sum_{l=1}^{L} N_l(\xi) P_{ml}, \quad m = 1,2,...,M; \quad L = 6 \text{ or } 8, \quad (11)$$

$$\frac{\partial P_m}{\partial n_q}(\xi) = \sum_{l=1}^{L} N_l(\xi) \frac{\partial P_{ml}}{\partial n_q},$$
$$m = 1,2,...,M; \quad L = 6 \text{ or } 8, \quad (12)$$

where x_{il} is the ith coordinate component of the lth node; $N_l(\xi)$ are the quadratic shape functions;[12] $\xi \equiv (\xi_1,\xi_2)$ are the local coordinates; P_{ml} and $\partial P_{ml}/\partial n_q$ are the sound pressure and pressure gradient of the lth node on the mth element; and M is the total number of elements. The interpolation scheme is required only for the source surface, but not for the hologram. Substituting Eqs. (10)–(12) into Eqs. (2) and (5) gives the following discretized boundary integral equations:

$$\alpha p(\mathbf{x}_p) = \sum_{m=1}^{M} \left[\left(\int_{\Delta S_m} \frac{\partial G}{\partial n_q}(\mathbf{x}_p,\mathbf{x}_q(\xi)) J(\xi) \mathbf{N}(\xi) dS_q \right) \mathbf{P}_m \right.$$
$$\left. - \left(\int_{\Delta S_m} G(\mathbf{x}_p,\mathbf{x}_q(\xi)) J(\xi) \mathbf{N}(\xi) dS_q \right) (\mathbf{P}_n)_m \right], \quad (13)$$

and

$$\alpha \frac{\partial p}{\partial n_p}(\mathbf{x}_p)$$
$$= \sum_{m=1}^{M} \left[\left(\int_{\Delta S_m} \frac{\partial^2 G}{\partial n_p \partial n_q}(\mathbf{x}_p,\mathbf{x}_q(\xi)) \right. \right.$$
$$\left. \times J(\xi) \mathbf{N}(\xi) dS_q \right) \mathbf{P}_m - \left(\int_{\Delta S_m} \frac{\partial G}{\partial n_p}(\mathbf{x}_p,\mathbf{x}_q(\xi)) \right.$$
$$\left. \left. \times J(\xi) \mathbf{N}(\xi) dS_q \right) (\mathbf{P}_n)_m \right], \quad (14)$$

where ΔS_m is the area of the mth element; $J(\xi)$ is the Jacobian of the coordinate transformation; $\mathbf{N}(\xi)$ is an $1 \times L$ row

vector with $N_l(\xi)$ as its components; $\mathbf{P}_m$ and $(\mathbf{P}_n)_m$ are $L \times 1$ column vectors corresponding to P_{ml} and $\partial P_{ml}/\partial n_q$ in the integral equations. If there are M boundary elements and N nodes on the source surface, Eqs. (13) and (14) can eventually be assembled into the following matrix forms:

$$\alpha p(\mathbf{x}_p) = \left(\int_{\Delta S_m} \frac{\partial G}{\partial n_q} J \mathbf{N} \, dS_q \right)^{ps} \mathbf{P}^s$$

$$- \left(\int_{\Delta S_m} G J \mathbf{N} \, dS_q \right)^{ps} \mathbf{P}_n^s, \qquad (15)$$

$$\alpha \frac{\partial p}{\partial n_p}(\mathbf{x}_p) = \left(\int_{\Delta S_m} \frac{\partial G}{\partial n_p \partial n_q} J \mathbf{N} \, dS_q \right)^{ps} \mathbf{P}^s$$

$$- \left(\int_{\Delta S_m} \frac{\partial G}{\partial n_p} J \mathbf{N} \, dS_q \right)^{ps} \mathbf{P}_n^s. \qquad (16)$$

Or, in operator notations,

$$\alpha p(\mathbf{x}_p) = \mathbf{D}^{ps}\mathbf{P}^s - \mathbf{S}^{ps}\mathbf{P}_n^s, \qquad (17)$$

$$\alpha \frac{\partial p}{\partial n_p}(\mathbf{x}_p) = \mathbf{D}_n^{ps}\mathbf{P}^s - \mathbf{K}^{ps}\mathbf{P}_n^s, \qquad (18)$$

where $\mathbf{P}^s$ and $\mathbf{P}_n^s$ are $N \times 1$ row vectors corresponding, respectively, to the sound pressure $p(\mathbf{x}^s)$ and the pressure gradient $\partial p(\mathbf{x}^s)/\partial n_q$ of the N nodes $\mathbf{x}^s$; $\mathbf{S}^{ps}$, $\mathbf{D}^{ps}$, $\mathbf{K}^{ps}$, and $\mathbf{D}_n^{ps}$ are $1 \times N$ row vectors corresponding to the integrals in the square brackets of Eqs. (15) and (16). Superscript ps denotes the spatial transformation from the field point $\mathbf{x}_p$ to the source points $\mathbf{x}^s$.

Apparently, from Eqs. (17) and (18), the backward reconstruction of the sound pressure $p(\mathbf{x}^s)$ and the pressure gradient $\partial p(\mathbf{x}^s)/\partial n_q$ on the source surface [based on $p(\mathbf{x}^h)$ or $\partial p(\mathbf{x}^h)/\partial n$ measured on hologram S_h] is necessary before $p(\mathbf{x}_p)$ and $\partial p(\mathbf{x}_p)/\partial n_p$ at any field point $\mathbf{x}_p$ can be determined.

B. The BEM-based acoustic holography algorithms

Four BEM-based acoustic holography algorithms are presented in this section on the basis of the discretized boundary integral equations (17) and (18). These algorithms are developed for backward reconstruction and forward propagation of the sound fields radiated by irregularly shaped sources.

Assume that the sound pressure data $p(\mathbf{x}^h)$ are measured on N locations of the hologram S_h. The integral equation relating the source surface and the hologram is discretized and assembled into the matrix form as in Eq. (17) with $\alpha = 1$:

$$\mathbf{P}^h = \mathbf{D}^{hs}\mathbf{P}^s - \mathbf{S}^{hs}\mathbf{P}_n^s, \qquad (19)$$

where $\mathbf{P}^h$, $\mathbf{P}^s$, and $\mathbf{P}_n^s$ are $N \times 1$ column vectors corresponding to the given sound pressure $p(\mathbf{x}^h)$ and the unknown sound pressure $p(\mathbf{x}^s)$ and its gradient $\partial p(\mathbf{x}^s)/\partial n_q$; the superscript h and s denote, respectively, the hologram S_h and the source surface S_s; the subscript n denotes the directional derivative; $\mathbf{D}^{hs}$ and $\mathbf{S}^{hs}$ are both $N \times N$ square matrices corresponding to the integrals in Eq. (13) that relate the N measuring points $\mathbf{x}^h$ and the N surface nodes $\mathbf{x}^s$; the superscript

hs denotes a spatial transformation between the hologram S_h and the source surface S_s.

Boundary integral equation (17) with $\alpha = 1/2$ or $\Omega/4\pi$ (depending on whether the source surface is smooth or not) takes the following matrix form if the field point is taken to the source surface S_s:

$$\alpha \mathbf{P}^s = \mathbf{D}^{ss}\mathbf{P}^s - \mathbf{S}^{ss}\mathbf{P}_n^s \qquad (20)$$

or

$$\overline{\mathbf{D}}^{ss}\mathbf{P}^s = \mathbf{S}^{ss}\mathbf{P}_n^s, \qquad (21)$$

where $\mathbf{D}^{ss}$ and $\mathbf{S}^{ss}$ are both $N \times N$ square matrices corresponding to the integrals in Eq. (13) that relate the N field points and the N nodes $\mathbf{x}^s$ on source surface S_s; the superscript ss denotes both the field points and source points which are located on the source surface S_s, $\overline{\mathbf{D}}^{ss} \equiv (\mathbf{D}^{ss} - \alpha \mathbf{I})$, with $\mathbf{I}$ being an identity matrix.

Equations (19) and (21), respectively, constitute the main equation and the constraint equation with which one performs backward reconstruction of the sound field for irregularly shaped sources. This technique is termed pressure-based conformal holography with a hologram and a source surface coupling (PCHHS), since its formulation is based on the sound pressure measured on the hologram.

Two different ways of solving the unknowns $\mathbf{P}^s$ and $\mathbf{P}_n^s$ in Eqs. (19) and (21) exist. First, one may combine these two sets of equations into a single linear system with $2N$ equations and $2N$ unknowns. Second, one may substitute the constraint Eq. (21) into the main Eq. (19) to yield a single linear system with N equations and N unknowns. The second approach is adopted here because it requires less memory space and produces better-conditioned matrices than the first approach. That is,

$$[\mathbf{D}^{hs}(\overline{\mathbf{D}}^{ss})^{-1}\mathbf{S}^{ss} - \mathbf{S}^{hs}]\mathbf{P}_n^s = \mathbf{P}^h, \qquad (22)$$

with $\mathbf{P}^s$ eliminated. $\mathbf{P}^s$ can then be recovered from Eq. (21) after $\mathbf{P}_n^s$ is solved in Eq. (22). One may alternatively eliminate $\mathbf{P}_n^s$ from Eqs. (19) and (21) to obtain

$$[\mathbf{D}^{hs} - \mathbf{S}^{hs}(\mathbf{S}^{ss})^{-1}\overline{\mathbf{D}}^{ss}]\mathbf{P}^s = \mathbf{P}^h. \qquad (23)$$

$\mathbf{P}_n^s$ can then be recovered from Eq. (21) after $\mathbf{P}^s$ is solved in Eq. (23).

In some cases, it is more desirable to measure the sound pressure gradient, or equivalently, the particle velocity, by using an intensity probe. This situation arises when, for example, one seeks to avoid the influences from disturbing sources from the background in carrying out an acoustic measurement. This application motivates the development of the following velocity-based conformal holography with a hologram and a source surface coupling (VCHHS).

Suppose that the sound pressure gradient $\partial p(\mathbf{x}^h)/\partial n$, or the particle velocity $v_n(\mathbf{x}^h)$, is measured at N locations on the hologram. The integral equation relating the source surface and the hologram then takes the matrix form as in Eq. (18) with $\alpha = 1$:

$$\mathbf{P}_n^h = \mathbf{D}_n^{hs}\mathbf{P}^s - \mathbf{K}^{hs}\mathbf{P}_n^s, \qquad (24)$$

where $\mathbf{P}_n^h$ is an $N \times 1$ column vector corresponding to the known quantity $\partial p(\mathbf{x}^h)/\partial n$; $\mathbf{D}_n^{hs}$ and $\mathbf{K}^{hs}$ are both $N \times N$ square matrices corresponding to the integrals in Eq. (14)

that relate the N measuring points $\mathbf{x}^h$ and the N surface nodes $\mathbf{x}^s$. As with the pressure-based conformal holography, Eq. (21) can be used again as a constraint equation for eliminating the unknowns $\mathbf{P}_s$ from the main equation (24) to arrive at a linear system with N equations and N unknowns:

$$[\mathbf{D}_n^{hs}(\overline{\mathbf{D}}^{ss})^{-1}\mathbf{S}^{ss} - \mathbf{K}^{hs}]\mathbf{P}_n^s = \mathbf{P}_n^h. \tag{25}$$

Here, $\mathbf{P}^s$ can then be recovered from Eq. (21) after $\mathbf{P}_n^s$ is solved in Eq. (25). One may alternatively eliminate $\mathbf{P}_n^s$ from Eq. (24) to obtain

$$[\mathbf{D}_n^{hs} - \mathbf{K}^{hs}(\mathbf{S}^{ss})^{-1}\overline{\mathbf{D}}^{ss}]\mathbf{P}^s = \mathbf{P}^h. \tag{26}$$

Then $\mathbf{P}_n^s$ can then be recovered from Eq. (21) after $\mathbf{P}^s$ is solved in Eq. (26).

In addition to the previously mentioned algorithms that utilize the source surface integral as a constraint, an arbitrarily chosen surface located in the interior of the source may be used for setting up a constraint equation (see Fig. 1). This interior surface is only a fictitious one which is not required to be physically accessible in field measurement. One advantage of choosing an interior surface instead of a source surface as a constraint is: the integration kernels can never become singular when using the interior surface since the distances between the source points and field points are always greater than zero. Slow convergence in carrying out Gaussian quadrature integration for singular elements is then avoided to some degree. The choice of interior points is arbitrary, except for those points coinciding with the nodal points of the eigenmodes of the corresponding interior problems. Interior points with N pressure data measured on the hologram are chosen here to be located at equal distances along the inward normal directions to the source surface points. N interior points are thus located on a surface that almost conforms to the source surface. The following pres-

sure-based matrix equation is obtained here in accordance with the Helmholtz integral equation (18) with $\alpha = 0$:

$$\mathbf{D}^{is}\mathbf{P}^s = \mathbf{S}^{is}\mathbf{P}_n^s, \tag{27}$$

where $\mathbf{P}^s$ and $\mathbf{P}_n^s$ are defined in Eq. (19); $\mathbf{D}^{is}$ and $\mathbf{S}^{is}$ are both $N \times N$ square matrices corresponding to the integrals in Eq. (13) that relate the N field points and the N nodes $\mathbf{x}^s$ on the source surface S_s; the superscript is denotes the spatial transformation between the interior surface S_i and the source surface S_s.

Parallel to the development of the aforementioned two algorithms, the matrix Eq. (27) can be used as a constraint equation for eliminating either the unknown surface pressure $\mathbf{P}^s$, or the surface pressure gradient $\mathbf{P}_n^s$, from the main Eq. (19) to solve for the remaining unknown quantity. This approach is then termed pressure-based conformal holography with a hologram and a source interior coupling (PCHHI).

Similar reasoning can finally be applied to obtain a holography transformation algorithm based on the sound particle velocity $\mathbf{P}_n^h$ measured on the hologram, by using the source interior equation (27) as a constraint. One may choose to eliminate either the surface pressure $\mathbf{P}^s$ or the surface pressure gradient $\mathbf{P}_n^s$ to recover the other variable. This approach leads to velocity-based conformal holography with a hologram and a source interior coupling (VCHHI).

The resulting matrix equations of these four acoustic holography algorithms (with the different types of constraints presented in this section) are summarized in Table I. Backward reconstruction and forward propagation of the sound pressure, the particle velocity, and the sound intensity at any field point of interest can be performed by applying either the pressure-based approach or the velocity-based approach.

TABLE I. Summary of the BEM-based acoustic holography algorithms.

Model	Known	Unknown	Fundamental matrix equations	Variable eliminated	Resultant system equations
PCHHS	$\mathbf{p}^h$		main equation: $\mathbf{P}^h = \mathbf{D}^{hs}\mathbf{p}^s - \mathbf{S}^{hs}\mathbf{p}_n^s$	$\mathbf{p}^s$	$[\mathbf{D}^{hs}(\overline{\mathbf{D}}^{ss})^{-1}\mathbf{S}^{ss} - \mathbf{S}^{hs}]\mathbf{p}_n^s = \mathbf{p}^h$
			constraint equation: $\overline{\mathbf{D}}^{ss}\mathbf{p}^s = \mathbf{S}^{ss}\mathbf{p}_n^s$	$\mathbf{p}_n^s$	$[\mathbf{D}^{hs} - \mathbf{S}^{hs}(\mathbf{S}^{ss})^{-1}\overline{\mathbf{D}}^{ss}]\mathbf{p}^s = \mathbf{p}^h$
VCHHS	$\mathbf{p}_n^h$		main equation: $\mathbf{P}_n^h = \mathbf{D}_n^{hs}\mathbf{p}^s - \mathbf{K}^{hs}\mathbf{p}_n^s$	$\mathbf{p}^s$	$[\mathbf{D}_n^{hs}(\overline{\mathbf{D}}^{ss})^{-1}\mathbf{S}^{ss} - \mathbf{K}^{hs}]\mathbf{p}_n^s = \mathbf{p}_n^h$
		$\mathbf{p}^s$	constraint equation: $\overline{\mathbf{D}}^{ss}\mathbf{p}^s = \mathbf{S}^{ss}\mathbf{p}_n^s$	$\mathbf{p}_n^s$	$[\mathbf{D}_n^{hs} - \mathbf{K}^{hs}(\mathbf{S}^{ss})^{-1}\overline{\mathbf{D}}^{ss}]\mathbf{p}^s = \mathbf{p}_n^h$
PCHHI	$\mathbf{p}^h$	and $\mathbf{p}_n^s$	main equation: $\mathbf{P}^h = \mathbf{D}^{hs}\mathbf{p}^s - \mathbf{S}^{hs}\mathbf{p}_n^s$	$\mathbf{p}^s$	$[\mathbf{D}^{hs}(\mathbf{D}^{is})^{-1}\mathbf{S}^{is} - \mathbf{S}^{hs}]\mathbf{p}_n^s = \mathbf{p}^h$
			constraint equation: $\mathbf{D}^{is}\mathbf{p}^s = \mathbf{S}^{is}\mathbf{p}_n^s$	$\mathbf{p}_n^s$	$[\mathbf{D}^{hs} - \mathbf{S}^{hs}(\mathbf{S}^{is})^{-1}\mathbf{D}^{is}]\mathbf{p}^s = \mathbf{p}^h$
VCHHI	$\mathbf{p}_n^h$		main equation: $\mathbf{P}_n^h = \mathbf{D}_n^{hs}\mathbf{p}^s - \mathbf{K}^{hs}\mathbf{p}_n^s$	$\mathbf{p}^s$	$[\mathbf{D}_n^{hs}(\mathbf{D}^{is})^{-1}\mathbf{S}^{is} - \mathbf{K}^{hs}]\mathbf{p}_n^s = \mathbf{p}_n^h$
			constraint equation: $\mathbf{D}^{is}\mathbf{p}^s = \mathbf{S}^{is}\mathbf{p}_n^s$	$\mathbf{p}_n^s$	$[\mathbf{D}_n^{hs} - \mathbf{K}^{hs}(\mathbf{S}^{is})^{-1}\mathbf{D}^{is}]\mathbf{p}^s = \mathbf{p}_n^h$

Some noteworthy numerical aspects arise in the implementation phase of the acoustic holography algorithms. The first aspect is associated with evaluation of the singular integrals. The assembled coefficient matrices in the aforementioned integral formulation, i.e., $\overline{\mathbf{D}}^{ss}$ and $\mathbf{S}^{ss}$, involve evaluation of singular integrals. Element integrals can be conveniently evaluated by using the Gaussian quadrature algorithm when the field point $\mathbf{x}_p$ and the source point $\mathbf{x}_q$ are apart from each other. Integrands become singular when the field point $\mathbf{x}_p$ coincides with the source point $\mathbf{x}_q$. Singularity of the integrand can be reduced by means of polar transformation in order to improve convergence in carrying out the Gaussian quadrature integration. This is a typical procedure detailed in BEM literature.[12,13]

The second numerical aspect is associated with the treatment of nonsmooth source surfaces. Recall that the parameter α in Eq. (2) equals 1/2 for smooth source surfaces and $\Omega/4\pi$ for nonsmooth surfaces. Direct calculation of the solid angle Ω usually poses difficulties. This can easily be circumvented by applying uniform potential to the interior domain:[18]

$$\alpha_p = 1 + \frac{1}{4\pi} \sum_{m=1}^{M} \int_{\Delta S_m} \frac{\partial}{\partial n_q} \left(\frac{1}{|\mathbf{x}_p - \mathbf{x}_q(\xi)|} \right) J(\xi) dS_q(\xi). \tag{28}$$

The third numerical aspect is associated with how to handle the ill-posed nature resulting from the matrix inversion in backward reconstruction of source fields. Because wave propagation *per se* is a blurring process, the rapidly varying wave contents (termed evanescent waves) decay as sound waves propagate to the far field. Two distinct source fields are likely to be mapped into nearly identical hologram images and cause numerical nonuniqueness. To reconstruct the details of a source field (based on a blurred hologram field) is in general very difficult in cases of large distance of transformation. This ill-posed nature leads to nearly singular matrices in the calculation of holography transformation. Direct inversion of linear equations of this kind will inevitably amplify numerical errors, as well as measurement errors contained in the hologram data, and will eventually produce disastrous results.

In order to alleviate the ill-posed nature, SVD[19,20] is incorporated into the holography transformation algorithms. Suppose that the discretized integral equations of the holography algorithms take the following matrix form:

$$\mathbf{Ax} = \mathbf{y}, \tag{29}$$

where $\mathbf{A}$ is an $N \times N$ coefficient matrix, $\mathbf{x}$ is an $N \times 1$ column vector containing the unknown quantities on the source surface, and $\mathbf{y}$ is an $N \times 1$ column vector containing the measured sound data on the hologram. It can be shown that a least-squares solution can be obtained from pseudo-inversion of the linear system in Eq. (29) by virtue of the SVD algorithm:[19,20]

$$\mathbf{x}_{ls} = \mathbf{A}^\dagger \mathbf{y} = (\mathbf{VS}^\dagger \mathbf{U}^h) \mathbf{y} \simeq \sum_{i=1}^{k} a_i v_i, \tag{30}$$

where h is the Hermitian conjugate operator, $\mathbf{U}$ and $\mathbf{V}$ are unitary matrices, $\mathbf{S}^\dagger$ is a diagonal matrix with $\{\mathbf{S}_{ii}^\dagger\} = 1/\sigma_i$ ($i = 1,2,...,r$; r is the rank of $\mathbf{A}$; σ_i are singular values) and

$\{\mathbf{S}_{ii}^\dagger\} = 0 (i = r + 1,...,N)$, and $a_i = 1/\sigma_i$ ($\mathbf{u}_i^h \mathbf{y}$) ($\mathbf{u}_i$ are the column vectors of $\mathbf{U}$, and k is the cutoff number). The cutoff number k, in practice, is set to be smaller than the rank r of the matrix $\mathbf{A}$ in order to trade numerical stability for image resolution. This is essentially analogous to the filtering process used in the FFT planar holography.[1,2]

III. VERIFICATION OF THE HOLOGRAPHY TRANSFORMATION METHODS

An extensive numerical simulation has been conducted to investigate the numerical performance of each BEM-based acoustic holography algorithm. The hologram is chosen in such a way that its surface nearly conforms to the source surface which is in turn approximated by M boundary elements with N colocation nodes $\mathbf{x}^s$. The scanned points on the hologram are selected by propagating away from the N source surface nodes $\mathbf{x}^s$ at equal distances along outward normal directions of the source surface. Assume that the sound pressure $\mathbf{P}^h$ and the pressure gradient $\mathbf{P}_n^h$ can be either experimentally measured or synthetically generated for locations specified on the hologram. The choice of nodes on a hologram and a source surface in this conformal manner is merely for numerical convenience and not a strict requirement. Depending on the type of hologram data, either the pressure-based algorithms or the velocity-based algorithms, with either a source surface constraint or an interior constraint, may be utilized to form a linear system of equations $\mathbf{Ax} = \mathbf{y}$. LU decomposition is then applied to determine the condition number of the matrix $\mathbf{A}$. The condition number 1×10^8, as a rule of thumb, is selected as a demarcation of whether Gauss elimination or SVD is to be used. The SVD algorithm, in conjunction with appropriate filtering, is required for backward reconstruction of the source field if the condition number of the coefficient matrix is greater than 1×10^8. Determining an appropriate cutoff number k before satisfactory results can be reached may take several times of trial and error. Forward propagation of the source field to any point of interest in a three-dimensional space can then be proceeded with if the sound data reconstructed on the source surface are acceptable.

A. The pulsating sphere

A pulsating sphere is selected as the first test sound source in the simulation, without taking advantage of the symmetry of its spherical sound field, for validating the holography transformation algorithms.

Consider a pulsating sphere of radius a whose surface vibrates radially with the velocity $U_a \exp(-\omega t)$. The sound pressure and particle velocity at the field point $\mathbf{x}_p$ at a distance r from the center of the sphere are expressed as[7]

$$p(\mathbf{x}_p) = \left(\frac{a}{r} \right) \rho c U_a \left(\frac{ika}{ika - 1} \right) \exp[ik(r - a)], \tag{31}$$

and

$$v_r(\mathbf{x}_p) = \left(\frac{a}{r} \right)^2 U_a \left(\frac{ikr - 1}{ika - 1} \right) \exp[ik(r - a)]. \tag{32}$$

The mesh of the sphere consists of 12 triangular elements and 6 quadrilateral elements with 44 colocation nodes (see

Fig. 3). Input parameters used in this simulation are $a = 0.3$ m, $U_a = 1$ m/s, $\rho = 1.19$ kg/m^3, $c = 343.5$ m/s, $k = 10$ m^{-1}, $\lambda = 0.623$ m, and $ka = 3$. Another concentric sphere of radius 0.4 m is chosen as the hologram. The distance of transformation (DOT), defined as the normal distance between the hologram and the source surface, is accordingly 0.1 m (0.16λ). Four holography transformation algorithms are then applied to calculate the sound pressure, the particle velocity, the active intensity, and the reactive intensity at the nodes on the dashed line of the mesh shown in Fig. 3. The holography results and the analytical solutions are compared in Fig. 4 and Table II. Good agreement (with an error less than 4%) is achieved with an 18-element and 44-node mesh. Each holography algorithm takes approximately 2 min CPU time on the VAX 8800 in carrying out the computations.

B. The pulsating cylinder with two spherical endcaps

A pulsating cylinder with spherical endcaps is selected as the second test sound source (see Fig. 5). The sound field on the source surface is synthetically generated as if there is a pulsating line source of finite length inside the cylinder. The reason for choosing this particular type of source field is that the analytical solution of the sound field radiated by a line source is numerically easy to obtain. In addition, the field pattern and directivity are also at one's disposal by varying the Helmholtz number kL (with L being the length of the embedded line source). Sound fields tend to be more directive and rapidly varying with large kL values than with small kL values. A simulation is conducted for verification of the holography transformation algorithms. This is done without taking advantage of the axial symmetry of the cylindrical source.

Consider a cylinder with spherical endcaps, containing in its interior a line source of finite length L and radius a, and with surface velocity U_0 (see Fig. 5). The length of the cylin-

drical part of the source is also L. The spherical endcaps are both of radius R_s. The sound pressure $p(\mathbf{x}_p)$ and the particle velocity $v_n(\mathbf{x}_p)$, along the direction $\mathbf{n}_p$, can be calculated by[21]
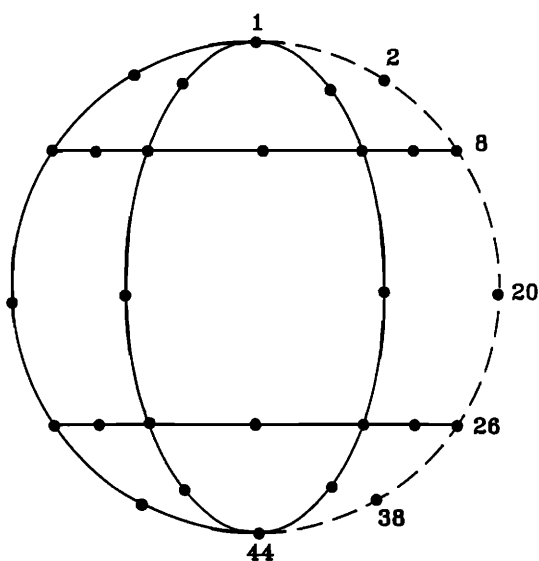
$$p(\mathbf{x}_p) = i \frac{\rho c U_0 ka}{2} \int_{-L/2}^{L/2} \frac{1}{r} e^{ikr} dz \qquad (33)$$

and

$$v_n(\mathbf{x}_p) = \frac{U_0 a}{2} \int_{-L/2}^{L/2} \frac{1}{r^2} (ikr - 1) e^{ikr} \frac{\partial r}{\partial n_p} dz, \qquad (34)$$

with r being the distance between the field point $\mathbf{x}_p$ and the source point $\mathbf{x}_q$. The input parameters are chosen in this simulation as $L = 0.5$ m, $a = 0.01$ m, $U_0 = 100$ m/s, $R_s = 0.3$ m, $\rho = 1.19$ kg/m^2, and $c = 343.5$ m/s. Nine simulation cases (see Table III) are designed for investigation of the numerical aspects of the acoustic holography algorithms, for example, the mesh spacing, the kL values, and the distance of transformation in reconstruction of the sound field radiated by the cylindrical source. Two types of meshes, with different sampling spacings, are used in the simulation (see Fig. 6). In the forward propagation cases, the field points $\mathbf{x}_p$ are located on a semicircle of radius 1 m on the XZ plane (see Fig. 7).
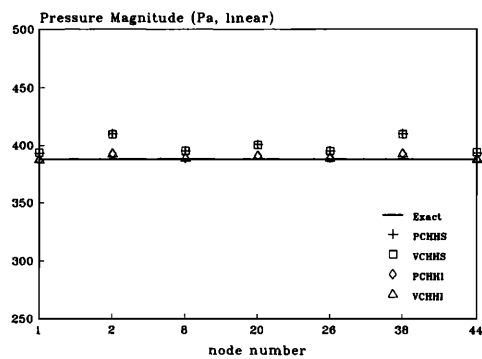
The results of the holography transformation algorithms are presented only for the nodes along the dashed lines of Fig. 6 because the sound field of the cylindrical source is axially symmetrical. Relative errors between the holography transformation results and the exact solutions computed by Eqs. (33) and (34) are summarized in Tables IV and V.

Figure 8 shows the results of the acoustic holography algorithms with DOT $= 0.16\, \lambda$ and a mesh containing 20 elements and 54 nodes (case 1 in Table III) for the sound pressure, the particle velocity, the active intensity, and the reactive intensity of the cylindrical source ($kL = 5$). Errors in the results are within approximately 5% and 6% for the pressure and the particle velocity, respectively (see case 1 in Table IV and V). Only slowly varying propagating waves are captured in the reconstruction process since the mesh used in this case is relatively coarse. Well-conditioned coefficient matrices, at the expense of poor resolution, can then be obtained so that the Gauss elimination algorithm can be directly applied.
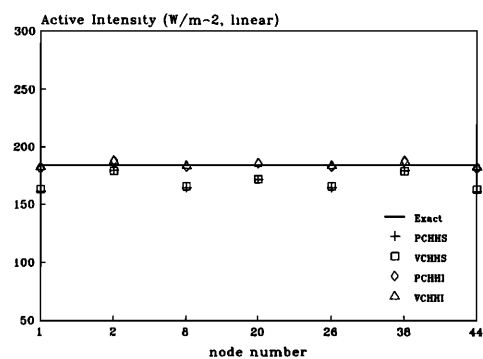
The effect of different mesh spacings on the holography transformation algorithms is investigated in cases 1 and 2. Only the results of the pressure magnitude (due to limited space) are shown in Fig. 9. The transformation using a finer mesh yields more accurate results as expected (approximately 1% vs 5% error in Table IV for cases 1 and 2, respectively).

The results of the holography algorithms with a source interior constraint, i.e., algorithms PCHHI and VCHHI, are significantly better than those obtained from the other two algorithms employing a source surface constraint. An explanation for this is that the holography algorithms with a source interior constraint do not require evaluation of singular elements since the distances between the field points and the source points can never become zero.
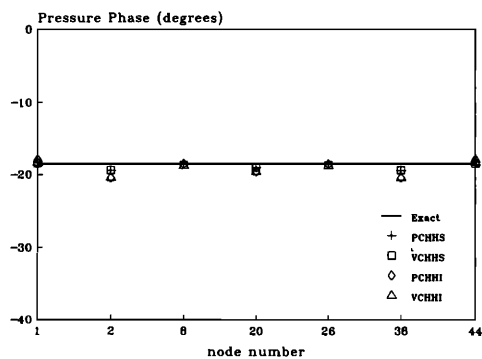
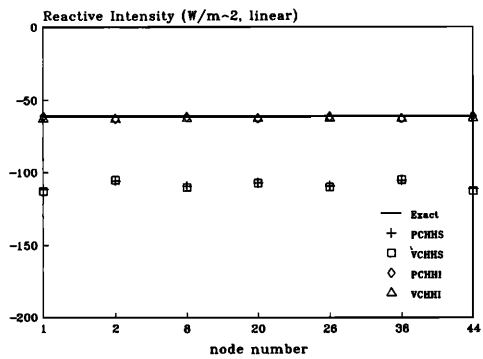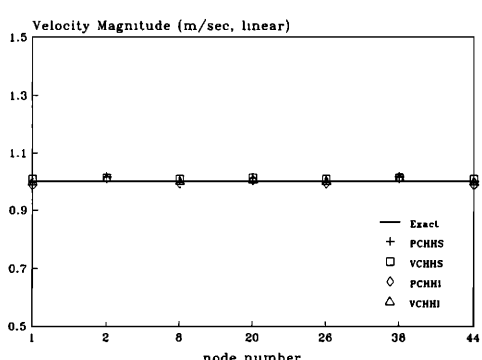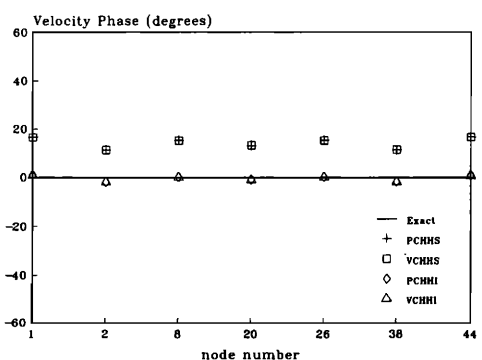The holographically transformed results of the back-

FIG. 3. Boundary mesh of a pulsating sphere (with 18 elements and 44 nodes).

Pressure Magnitude (Pa, linear)

— Exact
+ PCHHS
□ VCHHS
◊ PCHHI
△ VCHHI

node number
(a)

Pressure Phase (degrees)

— Exact
+ PCHHS
□ VCHHS
◊ PCHHI
△ VCHHI

node number
(b)

Velocity Magnitude (m/sec, linear)

— Exact
+ PCHHS
□ VCHHS
◊ PCHHI
△ VCHHI

node number
(c)

Velocity Phase (degrees)

— Exact
+ PCHHS
□ VCHHS
◊ PCHHI
△ VCHHI

node number
(d)

Active Intensity (W/m~2, linear)

— Exact
+ PCHHS
□ VCHHS
◊ PCHHI
△ VCHHI

node number
(e)

Reactive Intensity (W/m~2, linear)

— Exact
+ PCHHS
□ VCHHS
◊ PCHHI
△ VCHHI

node number
(f)

FIG. 4. Acoustic holography results versus exact solutions for the sound field radiated by a pulsating sphere ($ka = 3$). The holography calculation is based on an 18-element and 44-node mesh. The distance of transformation is 0.16 λ. The sound field is backward reconstructed on the source surface. (a) Pressure magnitude; (b) pressure phase; (c) particle velocity magnitude; (d) particle velocity phase; (e) active intensity; (f) reactive intensity.

TABLE II. The mean relative errors (%) of the sound-pressure magnitude and the particle velocity magnitude results reconstructed on the surface of the pulsating sphere shown in Fig. 3.

Model	PCHHS	VCHHS	PCHHI	VCHHI
Pressure magnitude	3.70	3.64	0.74	0.67
Velocity magnitude	1.00	1.10	0.76	0.48

ward reconstruction of a low-frequency field ($kL = 5$, case 2 in Table III) and a high-frequency field ($kL = 10$, case 6 in Table III), based on a 42-element and 116-node mesh, are compared in Fig. 10. The errors for the low-frequency field are smaller than those for the high-frequency field (approximately 1.3% vs 1.6% in Table IV for cases 2 and 6, respectively), because the smooth and divergent fields radiated by low-frequency sources can be reasonably represented by using coarse meshes.
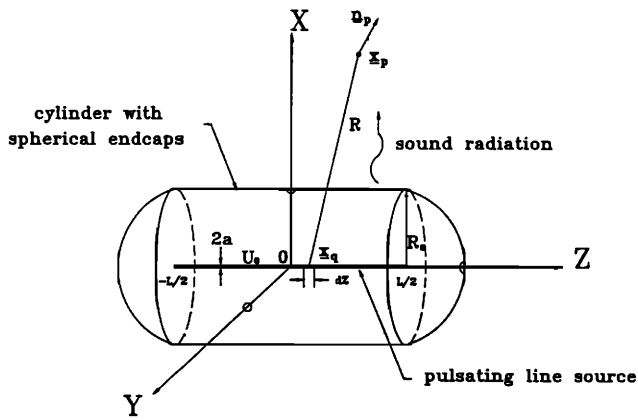
FIG. 5. Configuration of a cylinder with spherical endcaps embedded with a synthetic pulsating line source of finite length L and radius a.
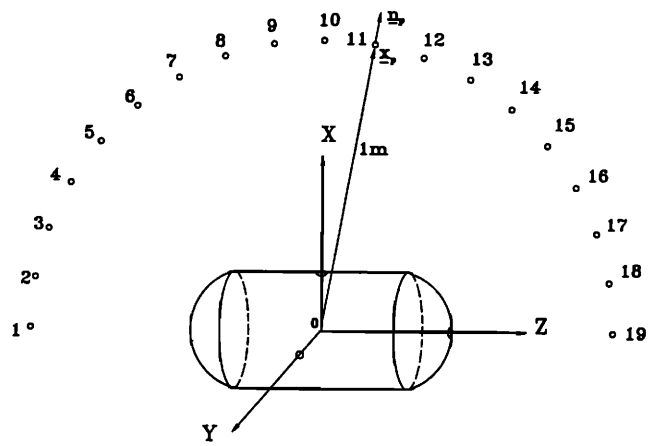

FIG. 7. Field points used in the forward propagation cases of the sound field radiated by a cylinder with spherical endcaps. Every field point is equally spaced on a semicircle of radius 1 m.

TABLE III. Holography transformation parameters used in the simulation cases of the sound field radiated by a cylinder with spherical endcaps shown in Fig. 5. [Note: (20,54) denotes a mesh with 20 elements and 54 nodes. GE denotes the Gauss elimination algorithm. SVD denotes the singular value decomposition algorithm.]

Case	Mesh	kL	DOT/λ	Solution method of $\mathbf{Ax} = \mathbf{v}$	Direction of transformation
1	(20,54)	5	0.16	GE	backward
2	(42,116)	5	0.16	GE	backward
3	(42,116)	5	0.16	GE	forward
4	(42,116)	5	4.77	SVD	backward
5	(42,116)	5	4.77	SVD	forward
6	(42,116)	10	0.32	GE	backward
7	(42,116)	10	0.32	GE	forward
8	(42,116)	10	9.55	SVD	backward
9	(42,116)	10	9.55	SVD	forward

TABLE IV. The mean relative errors (%) of the sound-pressure magnitude results reconstructed on the surface of the cylinder with spherical endcaps shown in Fig. 5.

Case	Holography transformation algorithms			
	PCHHS	VCHHS	PCHHI	VCHHI
1	4.68	4.45	1.03	1.14
2	1.33	1.29	0.61	0.56
3	0.01	0.01	0.01	0.01
4	2.55	2.56	2.28	2.15
5	0.04	0.04	0.04	0.04
6	1.63	1.59	2.18	2.09
7	0.12	0.15	0.12	0.17
8	4.70	4.56	5.69	4.62
9	1.42	1.44	1.40	1.42

FIG. 6. Boundary mesh of a cylinder with spherical endcaps. (a) Coarse mesh (20 elements and 54 nodes); (b) fine mesh (42 element and 116 nodes).

TABLE V. The mean relative errors (%) of the sound particle velocity magnitude results reconstructed on the surface of the cylinder with spherical endcaps shown in Fig. 5.
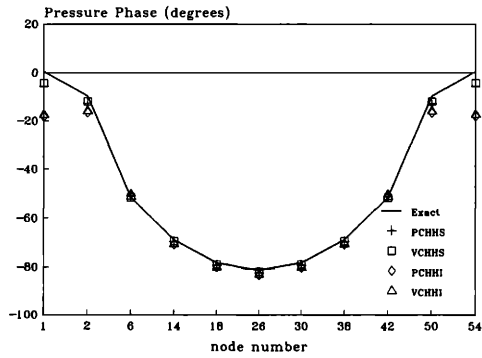
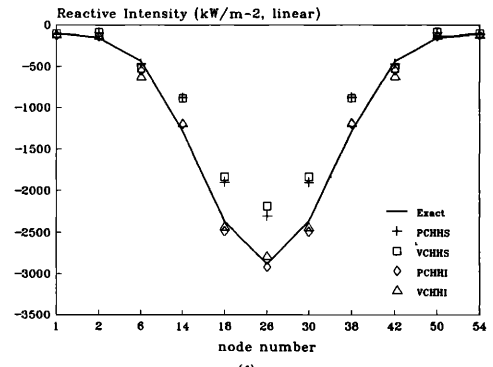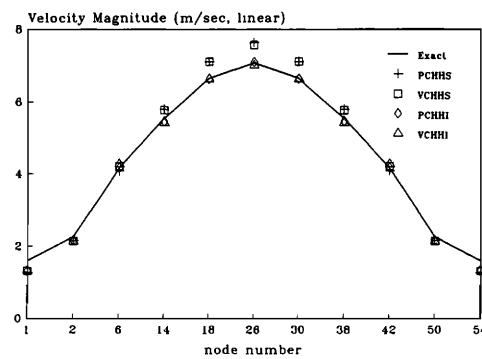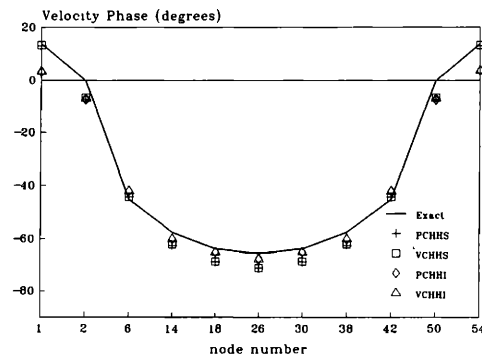| Case	Holography transformation algorithms			
	PCHHS	VCHHS	PCHHI	VCHHI
1	5.78	5.62	3.28	3.63
2	1.44	1.35	0.81	0.89
3	0.01	0.01	0.01	0.01
4	46.45	46.45	45.67	44.96
5	0.03	0.03	0.03	0.03
6	2.09	2.15	1.60	1.67
7	0.11	0.13	0.11	0.15
8	36.89	36.98	32.29	32.36
9	1.21	1.23	1.20	1.22
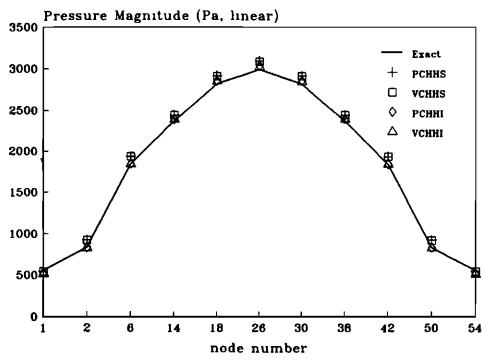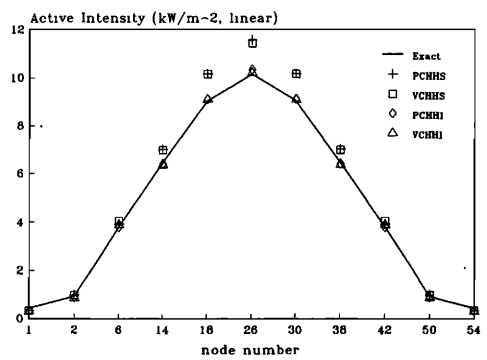
FIG. 8. Acoustic holography results versus exact solutions for the sound field radiated by a cylinder with spherical endcaps ($kL = 5$). The holography calculation is based on a 20-element and 54-node mesh. The distance of transformation is 0.16λ (case 1 in Table III). The sound field is backward reconstructed on the source surface. (a) Pressure magnitude; (b) pressure phase; (c) particle velocity magnitude; (d) particle velocity phase; (e) active intensity; (f) reactive intensity.

The forward propagation results obtained under the same conditions in cases 3 and 7 ($kL = 5$ and 10, respectively) are shown in Fig. 11. The sound fields of these two kL values are backward reconstructed on the cylindrical source surface. They are then forward propagated to the semicircle of Fig. 7. The error of the low-frequency case is smaller than that of the high-frequency case (approximately 0.01% vs

0.1% error in Table IV for cases 3 and 7, respectively). The forward propagation errors are significantly smaller than the backward reconstruction errors. Forward propagation is in general less difficult than backward reconstruction in conducting a holographical imaging because the former transformation is inherently a smoothing process that is insensitive to the reconstruction errors of the near field.

Pressure Magnitude (Pa, linear)

(a)

Pressure Magnitude (Pa, linear)

(a)

Pressure Magnitude (Pa, linear)

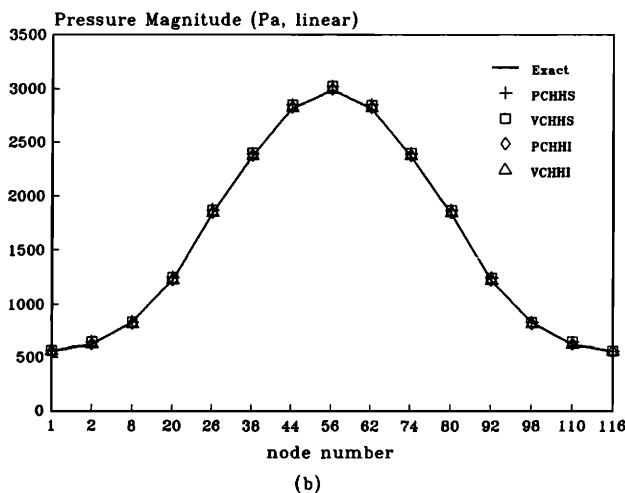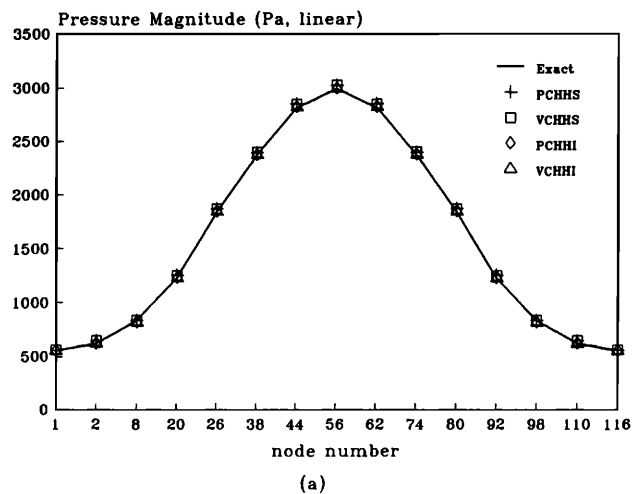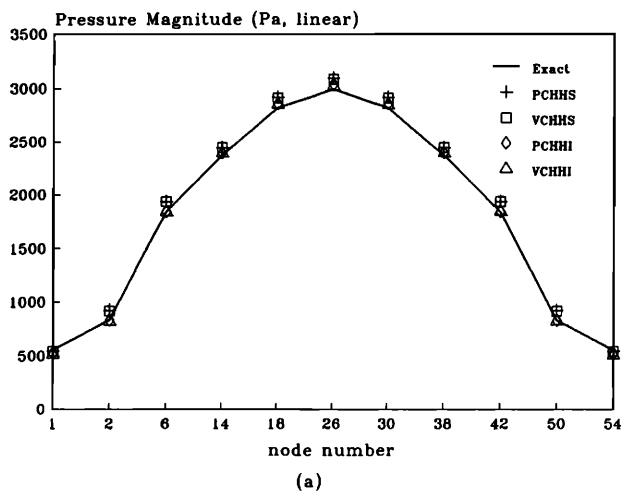(b)

Pressure Magnitude (kPa, linear)

(b)
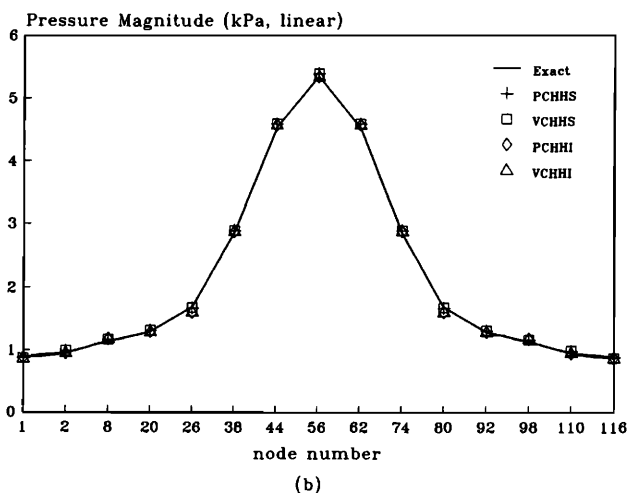
FIG. 9. Effect of mesh spacing on the acoustic holography. The pressure magnitude is backward reconstructed on the surface of a cylinder with spherical endcaps. (a) Holography transform result based on a 20-element and 54-node mesh (case 1 in Table III); (b) holography transform result based on a 42-element and 116-node mesh (case 2 in Table III).

FIG. 10. Effect of the sound field frequency on the acoustic holography. The pressure magnitude is backward reconstructed on the surface of a cylinder with spherical endcaps. The holography calculation is based on a 42-element and 116-node mesh. (a) Reconstructed result of a low-frequency field ($kL = 5$, case 2 in Table III); (b) reconstructed result of a high-frequency field ($kL = 10$, Case 6 in Table III).

The coefficient matrices resulting from the backward reconstruction process are well-conditioned because the distances of transformation are moderate in these cases (with the maximum 0.32 λ in case 7 of Table III). Satisfactory results in such cases can be obtained by direct application of the Gauss elimination algorithm to solve for the sound pressure or the particle velocity on the source surface. However, ill-posed nature is frequently encountered in backward reconstruction of source fields of large distance of transformation. The SVD algorithm is utilized to carry out pseudo-inversion of the hologram data in order to overcome this numerical difficulty. In addition, the filtering procedure is employed to ensure numerical stability, at the expense of the information contained in the high-order components of the decomposed field. Two backward reconstruction cases of large distance of transformation (DOT = 4.77 λ for case 4 and 9.55 λ for case 8 in Table III) are shown in Fig. 12. The

errors in the reconstructed sound pressure on the source surface, in spite of the incredibly large distances of transformation, are approximately 3% for the low-frequency field in case 4 ($kL = 5$) and 5% for the high-frequency field in case 8 ($kL = 10$), as shown in Table IV. The singular values obtained from the holography algorithms are plotted in Fig. 13. These singular values appear to be more uniformly distributed for high-frequency fields, which require more orthonormal modes of the decomposed field, than for low-frequency fields. As far as the filtering procedure is concerned, 75 and 100 out of 116 singular values are preserved for the low-frequency case 4 and the high-frequency case 8, respectively. The reconstruction errors for the particle velocity are significantly larger than the sound-pressure errors (approximately 46% for case 4 and 37% for case 8 in Tables IV and V). This is not entirely unexpected because, from the Euler's equation, differentiation from the sound pressure in obtaining the
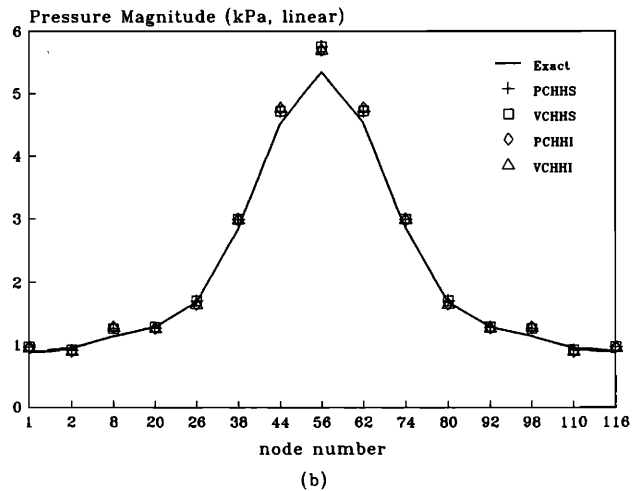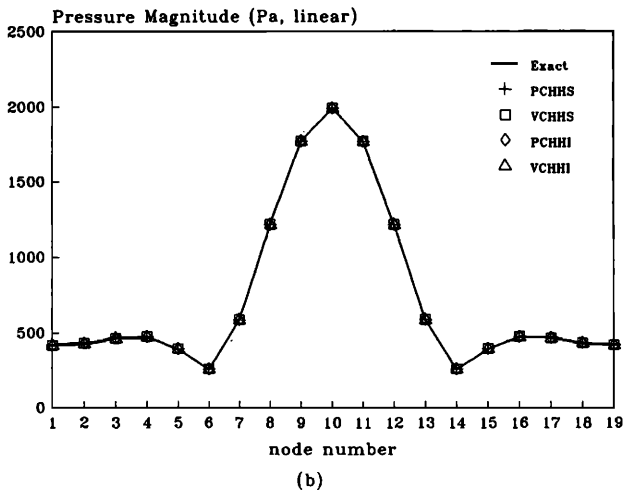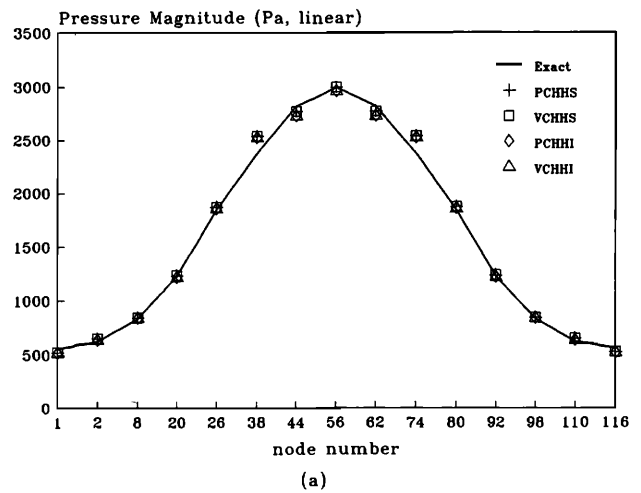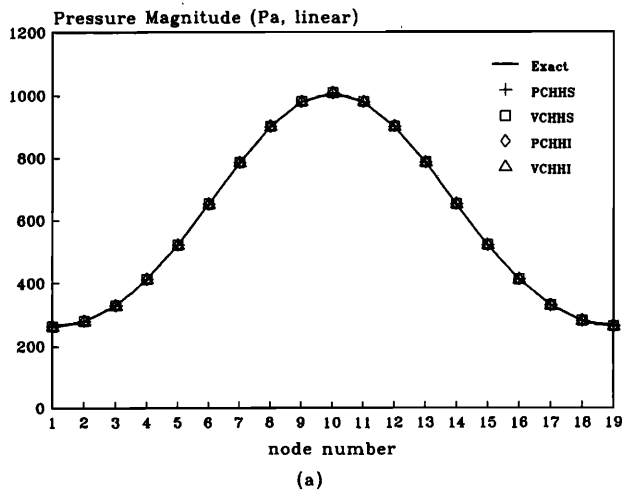
FIG. 11. Acoustic holography results versus exact solutions for the sound field radiated by a cylinder with spherical endcaps. The pressure magnitude is forward propagated to the image points of Fig. 7. The holography calculation is based on a 42-element and 116-node mesh. (a) Propagated result of a low-frequency field ($kL = 5$, Case 3 in Table III); (b) propagated result of a high-frequency field ($kL = 10$, case 7 in Table III).

FIG. 12. Effect of distance of transformation on acoustic holography. The pressure magnitude is backward reconstructed on the surface of a cylinder with spherical endcaps. The holography calculation is based on a 42-element and 116-node mesh. Singular value decomposition is used. (a) Distance of transformation $= 4.77 \lambda$, $kL = 5$, case 4 in Table III; (b) distance of transformation $= 9.55 \lambda$, $kL = 10$, case 8 in Table III.

particle velocity generally amplifies the errors contained in the former quantity.

In Fig. 14, the forward propagation results (DOT $= 4.77\lambda$ for case 5 and 9.55λ for case 9) are calculated by the holography algorithms based on the reconstructed fields obtained in cases 4 and 8. The results of holographically transformed sound pressure show satisfactory accuracy (approximately 0.1% for case 5 and 1% for case 9 in Table IV), despite the less accurate particle velocity field reconstructed on the source surface.

C. The vibrating piston set in a rigid sphere

In addition to the pulsating sphere and the cylinder with spherical endcaps, a more sophisticated source is adopted in the numerical simulation for verifying the BEM-based acoustic holography algorithms. A vibrating piston set in the

side of a rigid sphere of radius a is selected as the third test sound source (see Fig. 15). The spherical piston surface spans an angle θ_0 with respect to the z axis. The distribution of surface velocity is

$$U(a,\theta) = \begin{cases} U_0, & 0 < \theta < \theta_0 \\ 0, & \theta_0 < \theta < \pi. \end{cases}$$

The field pattern and directivity can be adjusted at will by varying the Helmholtz number ka and the spanning angle θ_0. Such a sound source provides a more rigorous test of the holography technique than the previous cases, because the field from the active part of the source must diffract around the object, with a significant decrease in information due to evanescent waves.

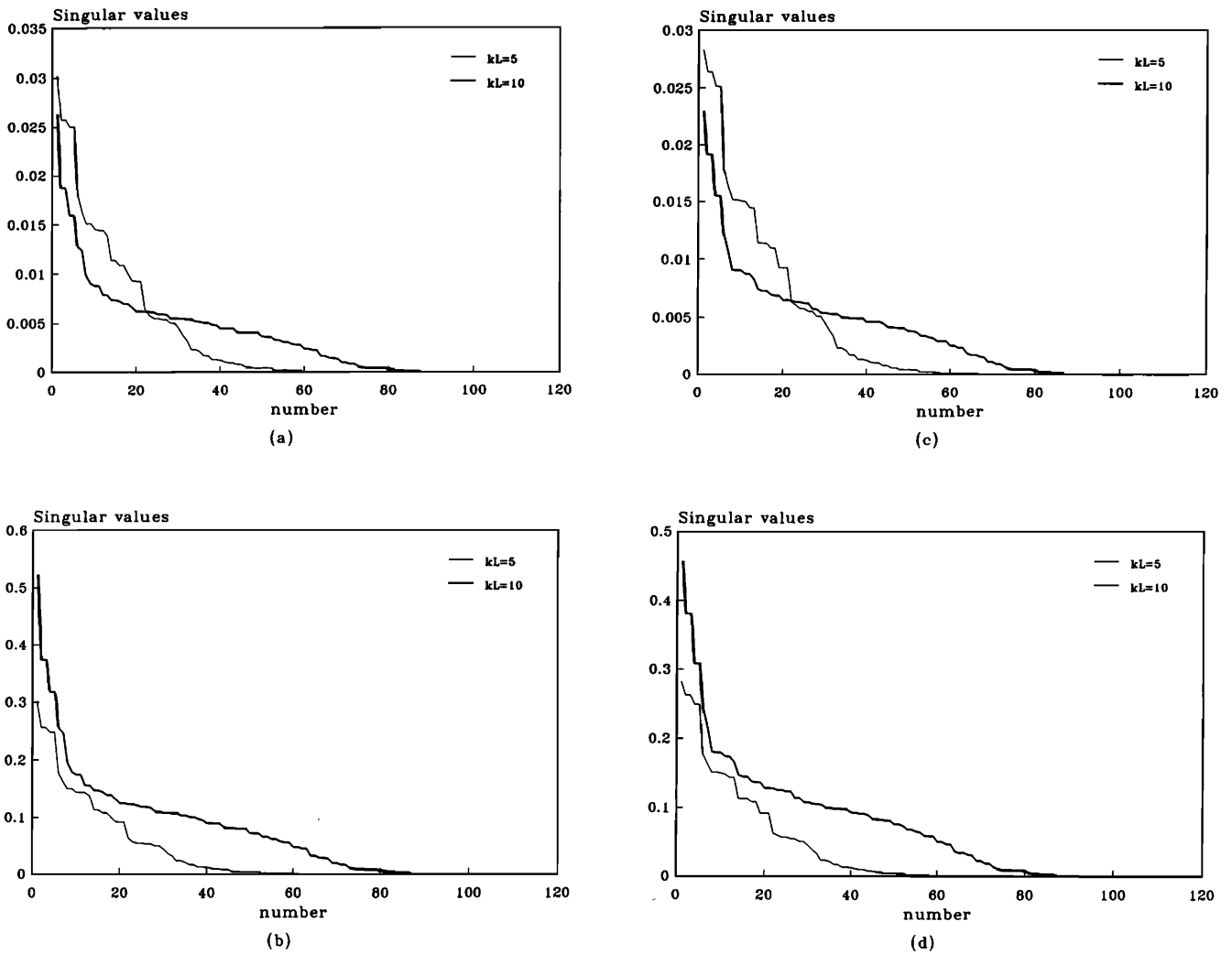The following analytical solution of a vibrating piston

FIG. 13. The singular values obtained for a low-frequency field ($kL = 5$, case 4 in Table III) and a high-frequency field ($kL = 10$, case 8 in Table III) when the sound field is backward reconstructed on the surface of a cylinder with spherical endcaps by using the following acoustic holography algorithms: (a) algorithm PCHHS; (b) algorithm VCHHS; (c) algorithm PCHHI; (d) algorithm VCHHI.

set in a rigid sphere is used to synthetically generate the sound-pressure field at a point (r,θ):[6]

$$p(r,\theta) = \sum_{m=0}^{\infty} \frac{i\rho c U_m}{h'_m(ka)} P_m(\cos\theta) h_m(kr), \qquad (35)$$

where

$$U_m = \tfrac{1}{2}U_0 \left[P_{m-1}(\cos\theta_0) - P_{m+1}(\cos\theta_0) \right], \qquad (36)$$

with P_m being the Legendre polynomial of degree m [$P_0(x) = 1$ and $P_1(x) = x$] and h_m being the spherical Bessel function of the first kind of order m. The first derivative of the spherical Bessel function in Eq. (35) is computed by the following recursive formula to keep truncation errors as small as possible:

$$h'_m(x) = \left[m h_{m-1}(x) - (m+1)h_{m+1}(x) \right]/(2m+1), \qquad (37)$$

with $h_0(x) = -i\exp(ix)/x$ and $h_1(x) = -\exp(ix) \times (x + i)/x^2$.

The input parameters used in the simulation of the piston set in a sphere are chosen as $a = 0.2$ m, $U_0 = 1$ m/s, $\rho = 1.19$ kg/m^3, and $c = 343.5$ m/s. Five simulation cases (see Table VI) are designed to investigate the numerical aspects of the acoustic holography algorithms, including the spanning angle θ_0, the distance of transformation, and the Helmholtz number ka. Without taking advantage of the axial symmetry of the piston, the holography transformation algorithms are applied to backward reconstruct the source field. A mesh with 18 elements and 44 nodes used for approximating the source is identical to the one shown in Fig. 3. Quadratic shape functions are again used for interpolating field variables.

The holographically transformed results are presented only for the nodes along the dashed line of Fig. 15, because the vibrating piston field is symmetrical about the z axis. Numerical results obtained from the holography transformation algorithms are compared to the analytical solutions in terms of polar plots from Figs. 16 to 20. The relative errors
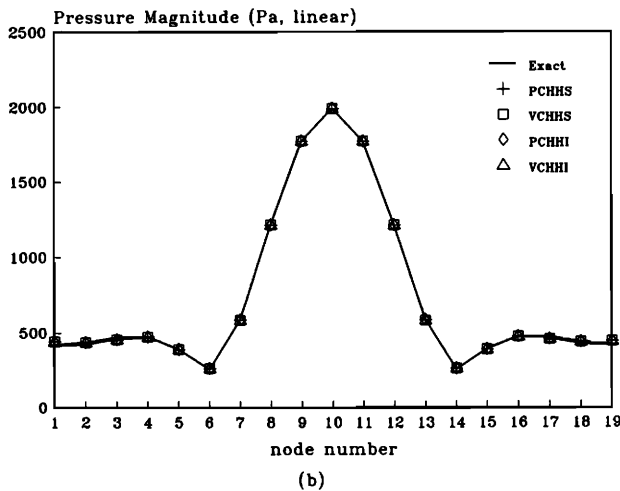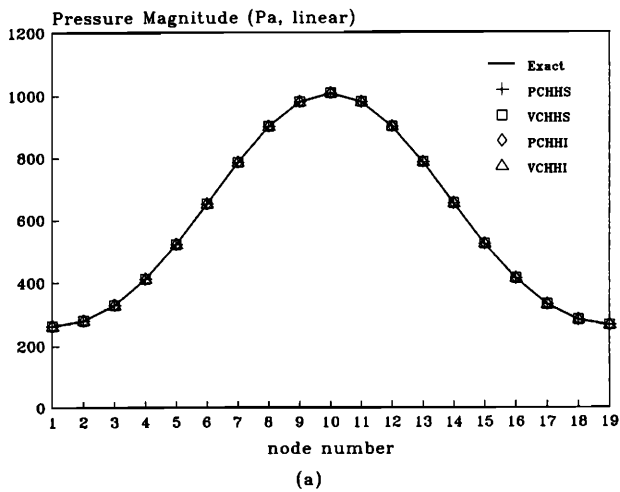
(a)

(b)

FIG. 14. Effect of distance of transformation on acoustic holography. The pressure magnitude is forward propagated to the far field of a pulsating cylinder with spherical endcaps after backward reconstruction on the source surface. The holography calculation is based on a 42-element and 116-node mesh. Singular value decomposition is used. (a) Distance of transformation $= 4.77\,\lambda$, $kL = 5$, case 5 in Table III; (b) distance of transformation $= 9.55\,\lambda$, $kL = 10$, case 9 in Table III.
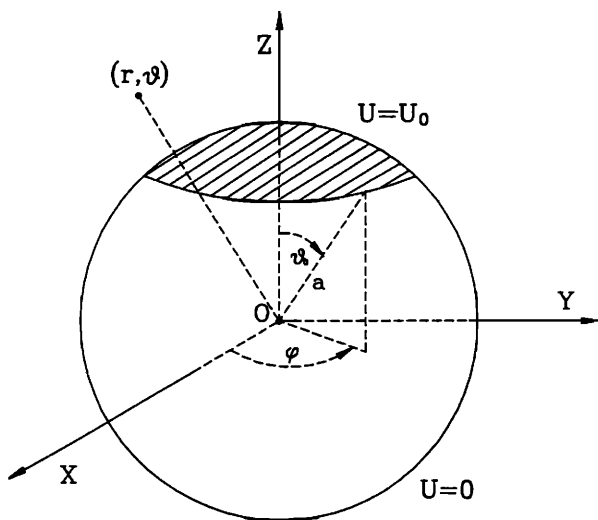

FIG. 15. Configuration of a vibrating piston spanned with an angle θ_0, set in a rigid sphere of radius a.

TABLE VI. Holography transformation parameters used in the simulation cases of the sound field radiated by a vibrating piston set in a rigid sphere shown in Fig. 15. (Note: Here, $a = 0.2$ m for all cases. DOT denotes the distance of backward reconstruction. SVD terms denotes the number of terms preserved in performing singular value decomposition.)

Case	ka	θ_0	DOT/λ	SVD terms
1	2	60°	0.16	44
2	2	30°	0.16	44
3	2	30°	0.16	44
4	2	30°	1.00	32
5	4	30°	0.16	44

between the transformed results and the exact solutions are summarized in Table VII. It can be observed from the reconstruction errors that this piston field is evidently more difficult to reconstruct than the previous cases.

In case 1, the holography transformation algorithms are applied to the vibrating piston set in a sphere, with a spanning angle $\theta_0 = 60°$ at a frequency 546.748 Hz ($ka = 2$). The source pressure field is backward reconstructed at a distance $1/6\,\lambda$ away from the source. The holographically transformed results and the exact solutions are compared in Fig. 16. The numerical results exhibit satisfactory accuracy, with relative errors less than 2.5% (see Table VII). The errors for the active part of the source are exaggerated because the graph is expressed in terms of the linear scale. The
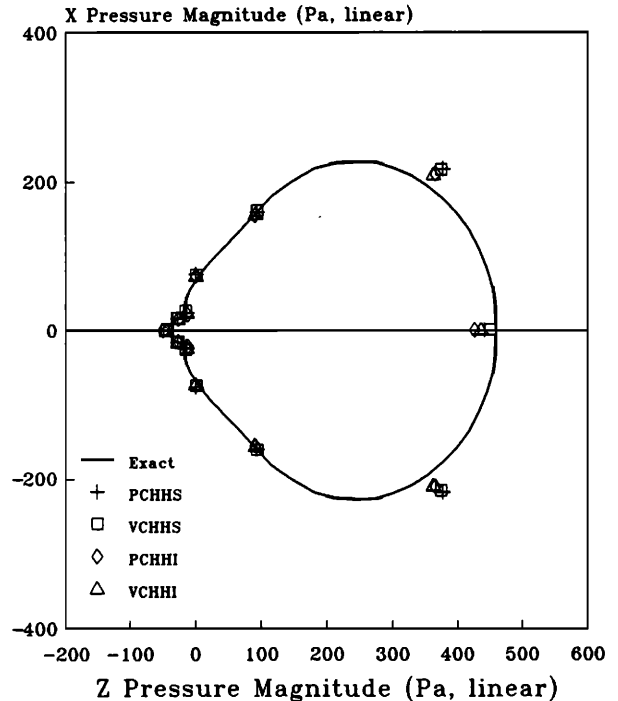

FIG. 16. Polar graph of the acoustic holography results versus exact solutions for the sound pressure radiated by a piston spanned by 60°, set in a sphere of radius 0.2 m ($ka = 2$). The holography calculation is based on an 18-element and 44-node mesh. The distance of transformation is 0.16 λ (case 1 in Table VI). The sound field is backward reconstructed on the source surface.
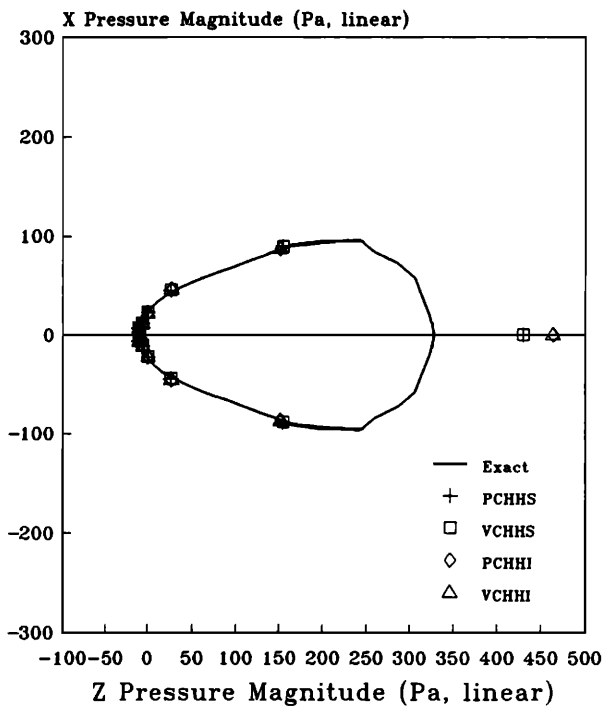
FIG. 17. Polar graph of acoustic holography results versus exact solutions for the sound pressure radiated by a piston spanned by 30°, set in a sphere of radius 0.2 m ($ka = 2$). The holography calculation is based on an 18-element and 44-node mesh. The distance of transformation is 0.16 λ (case 2 in Table VI). The sound field is backward reconstructed on the source surface.
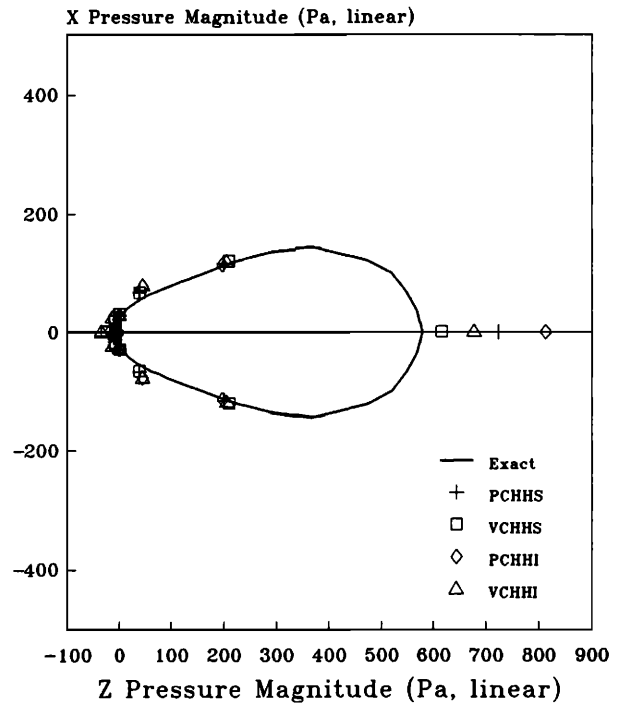

FIG. 19. Polar graph of acoustic holography results versus exact solutions for the sound pressure radiated by a piston spanned by 30°, set in a sphere of radius 0.2 m ($ka = 2$). The holography calculation is based on an 18-element and 44-node mesh. The distance of transformation is 1 λ (case 4 in Table VI). The sound field is backward reconstructed on the source surface. The SVD algorithm is invoked in the backward reconstruction process. Only 32 out of 44 singular values are preserved.
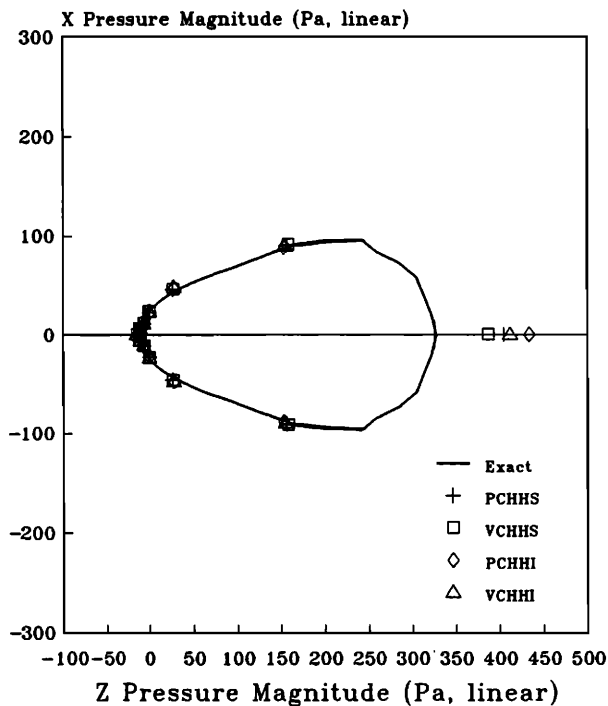

FIG. 18. Polar graph of acoustic holography results versus exact solutions for the sound pressure radiated by a piston spanned by 30°, set in a sphere of radius 0.2 m ($ka = 2$). The holography calculation is based on an 18-element and 44-node mesh. The distance of transformation is 1 λ (case 3 in Table VI). The sound field is backward reconstructed on the source surface.
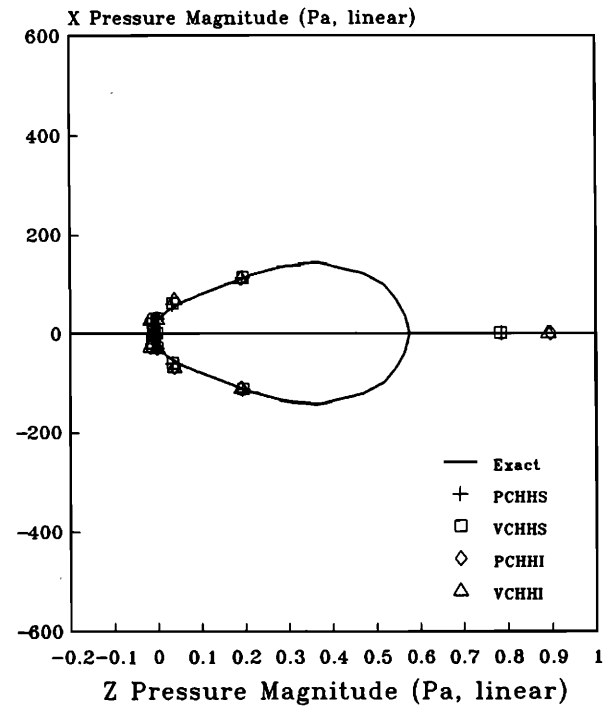

FIG. 20. Polar graph of acoustic holography results versus exact solutions for the sound pressure radiated by a piston spanned by 30°, set in a sphere of radius 0.2 m ($ka = 4$). The holography calculation is based on an 18-element and 44-node mesh. The distance of transformation is 0.16 λ (case 5 in Table VI). The sound field is backward reconstructed on the source surface.

TABLE VII. The mean relative errors (%) of the sound-pressure magnitude results reconstructed on the surface of the vibrating piston set in a sphere shown in Fig. 15.

| | Holography transformation algorithms | | | |
Case	PCHHS	VCHHS	PCHHI	VCHHI
1	2.16	2.50	1.08	0.66
2	14.69	12.20	18.90	15.83
3	17.45	17.43	22.26	22.24
4	10.01	9.98	10.65	10.61
5	20.01	10.95	31.86	20.48

algorithm VCHHS achieves the best performance among the methods utilized because its integration process for obtaining the sound pressure on the image surface (based on the particle velocity on the hologram) tends to smooth out numerical errors.

In case 2, the holography transformation algorithms are tested under a more difficult condition, with a smaller spanning angle $\theta_0 = 30°$. The field from the active part of the source must diffract around the sphere, with a significant decrease in information due to evanescent waves. The source pressure field is backward reconstructed at a distance $1/6\,\lambda$ away from the source. The transformed results and the exact solutions are compared in Fig. 17. There is, as expected, a significant increase in reconstruction errors (with a maximum of 18.9% in Table VII). Nevertheless, the backward reconstruction results (except for the active part of the source) appear acceptable for this more directive field.

In case 3, the distance of transformation is further increased to $1\,\lambda$, which is significantly larger than the previous $1/6\,\lambda$ in cases 1 and 2. The transformed results and the exact solutions are compared in Fig. 18. Sizable errors (with a maximum of 22.26%) arise due to ill-posed nature involved in the backward reconstruction process. This indicates that Gauss elimination is no longer recommended for this case. Therefore, in case 4, the SVD algorithm (in conjunction with appropriate filtering) is utilized to alleviate the numerical difficulty under the same test conditions as in case 3. Only 32 out of 44 singular values are preserved in this case for applying pseudo-inversion of the hologram data. Significant improvement can be observed in Fig. 19 and Table VII, with a maximum error of 10.65%. The velocity-based methods achieve a slightly better performance than the pressure-based methods.

An example of poor reconstruction is investigated in case 5 where the source frequency is increased to 1093.496 Hz ($ka = 4$). The source pressure field is reconstructed at a distance $1/6\,\lambda$ away from the source surface. The holographically transformed results and the exact solutions are compared in Fig. 20. The errors are summarized in Table VII, with a maximum error of 31.86% obtained from the algorithm PCHHI. In view of the poor quality of the reconstructed field, one may conclude that the mesh spacing ($1/3\,\lambda$) used in this case is too coarse to describe the details of the near field. This indicates that the $1/2$-λ rule commonly used in optical holography is obviously too broad a criterion for

choosing mesh spacings in applications of near-field acoustic holography.[1]

IV. CONCLUSION

Acoustic holography algorithms have been developed for spatial transformation of sound fields radiated by irregularly shaped sources which limit the use of conventional planar holography. The boundary element method, in conjunction with singular value decomposition, has been utilized to improve numerical efficiency as well as accuracy in performing spatial transformation. Satisfactory agreement between the holography results and the exact solutions exhibits the effectiveness of the BEM-based acoustic holography techniques.

Depending on field directivity, coarse meshes are sufficient for spatial transformation of the smooth and divergent fields radiated by low-frequency sources, while fine meshes are usually required to accurately represent the rapidly varying and convergent fields radiated by high-frequency sources.

The Gauss elimination algorithm suffices to solve the linear system of equations resulting from backward reconstruction of source fields in cases of moderate distances of transformation. However, singular value decomposition, in conjunction with appropriate filtering, is required for cases of large distances of transformation, in order to obtain acceptable reconstruction of source fields, at the expense of information contained in the high-order components of the decomposed field.

Future work will be focused on seeking optimal criteria for selecting the holography transformation parameters, for example, the mesh configuration, the distance of transformation, the cutoff number for singular values, the locations of the interior points. The BEM-based holography algorithms will also be extended to more realistic situations where interfering sources, background noise, or ground reflection are present in the measurement environment. This holography technique will be verified experimentally, especially for industrial applications associated with sound field characterization and noise source identification.

ACKNOWLEDGMENTS

[1] J. D. Maynard, E. G. Williams, and Y. Lee, "Nearfield Acoustic Holography: I. Theory of Generalized Holography and the Development of NAH," J. Acoust. Soc. Am. 78, 1395–1413 (1985).

[2] W. A. Veronesi and J. D. Maynard, "Nearfield Acoustic Holography (NAH): II. Holographic Reconstruction Algorithms and Computer Implementation," J. Acoust. Soc. Am. 81, 1307–1322 (1987).

[3] E. G. Williams and H. D. Dardy, "Generalized Nearfield Acoustical Holography for Cylindrical Geometry: Theory and Experiment," J. Acoust. Soc. Am. 81, 389–407 (1987).

[4] W. A. Veronesi and J. D. Maynard, "Digital Holographic Reconstruction of Sources with Arbitrarily Shaped Surfaces," J. Acoust. Soc. Am. 85, 588–598 (1989).

[5] Y. Huang, "Computer Techniques for Three-Dimensional Source Radiation," Ph.D. dissertation, Pennsylvania State University (1990).

[6] P. M. Morse and K. U. Ingard, *Theoretical Acoustics* (McGraw-Hill, New York, 1968).

[7] A. D. Pierce, *Acoustics* (McGraw-Hill, New York, 1981).

[8] G. F. Roach, *Green's Functions* (Cambridge U. P., New York, 1982).

[9] R. E. Kleimman and G. F. Roach, "Boundary Integral Equations for the Three-Dimensional Helmholtz Equation," SIAM Rev. **16**, 216–236 (1974).

[10] L. G. Kellogg, *Foundations of Potential Theory* (Springer-Verlag, Berlin, 1929).

[11] V. I. Smirnov, *A Course of Higher Mathematics* (Pergamon, Oxford, 1964).

[12] P. K. Banerjee and R. Butterfield, *Boundary Element Methods in Engineering Science* (McGraw-Hill, New York, 1981).

[13] C. A. Brebbia, *Boundary Element Techniques* (Springer-Verlag, Berlin, 1984).

[14] H. A. Schenck, "Improved Integral Formulation for Acoustic Radiation Problems," J. Acoust. Soc. Am. **44**, 42–58 (1968).

[15] A. J. Burton. and G. F. Miller, "The Application of Integral Equation Methods to the Numerical Solution of Some Exterior Boundary—Value Problems," Proc. R. Soc. London Ser. A **323**, 201–210 (1971).

[16] W. L. Meyer, W. A. Bell, B. T. Zinn, and M. P. Stallybrass, "Boundary Integral Solutions of Three Dimensional Acoustic Radiation Problems," J. Sound. Vib. **59**, 245–262 (1978).

[17] R. P. Shaw, "Boundary Integral Equation Method Applied to Wave Problems," in *Developments in Boundary Element Methods I*, edited by P. K. Banerjee and R. Butterfield (Appl. Sci., London, 1979), Chap. 6, pp. 121–153.

[18] A. F. Seybert, B. Spenarko, F. J. Rizzo, and D. J. Shippy, "An Advanced Computational Method for Radiation and Scattering of Acoustic Waves in Three Dimensions," J. Acoust. Soc. Am. **77**, 362–368 (1985).

[19] B. Noble and J. W. Daniel, *Applied Linear Algebra* (Prentice-Hall, Englewood Cliffs, NJ, 1988).

[20] W. K. Pratt, *Digital Image Processing* (Wiley, New York, 1982).

[21] L. E. Kinsler, A. R. Frey, A. B. Coppens, and J. V. Sanders, *Fundamentals of Acoustics* (Wiley, New York, 1982).